Journal of Alloys and Compounds 898 (2022) 162976

Contents lists available at ScienceDirect

Journal of Alloys and Compounds

journal homepage: www.elsevier.com/locate/jalcom

Crystal growth control of Ni-based alloys by modulation of the melt pool morphology in DED

Jiayun Shao[a,c], Gang Yu[a,b,c], Shaoxia Li[a,c], Xiuli He[a,c,*], Chongxin Tian[a,c,*], Binxin Dong[a,c]

[a] Institute of Mechanics, Chinese Academy of Sciences, Beijing 100190, China
[b] Center of Materials Science and Optoelectronics Engineering, University of Chinese Academy of Sciences, Beijing 100049, China
[c] School of Engineering Science, University of Chinese Academy of Sciences, Beijing 100049, China

ARTICLE INFO

Article history:
Received 22 September 2021
Received in revised form 15 November 2021
Accepted 25 November 2021
Available online 27 November 2021

Keywords:
Laser deposition
Crystal growth
Melt pool morphology
Ni-based superalloys

ABSTRACT

In additive manufacturing especially in directed energy deposition, it is hard to control crystal growth pattern due to the high temperature gradient in AM. Essentially, the crystal grows epitaxially from the substrate and columnar crystals with strong texture are exhibited in AM components. Here, small spot diameter was used for DED-L of Ni-based alloys and various crystal growth patterns were obtained by changing power density. Samples processed under low power density were shown to exhibit wide and shallow spindle-like melt pool, along with apparently hierarchical planar-columnar-equiaxed microstructure. While samples prepared under relatively high power density were shown to exhibit narrower and deeper melt pool with two sharp turning points, exhibiting inclined columnar grains and several discontinuous central axial columnar crystals. When highest power density and small spot diameter were applied, crystal growth with weak texture was achieved. Under this deep and narrow melt pool, the crystal growth can be separated into four regions: nearly-equiaxed grains with random grain orientations; horizontally symmetrically grown crystal grains; axial columnar in the center; columnar grains grew approximately vertical to the boundary of melt pool. Correlations were investigated between melt pool shape, solidification parameters and microstructure. The transformation of melt pool morphology was mainly attributed to the change of power density. Solidification parameters were shown to be different under different melt pool morphology. Diverse crystal growth patterns were achieved under different melt pool morphology controlled by power density, showing the feasibility of site-specific of microstructure control in DED-L according to the required mechanical properties.

1. Introduction

Additive manufacturing (AM), building three-dimensional parts layer-by-layer guided by a digital model, allows design and production of intricate and customized parts without the limitations of conventional processing techniques [1]. AM processes are categorized into Directed Energy Deposition (DED) and Powder bed Fusion (PBF) based on the powder delivery system. Compared with PBF, DED process delivers powder directly to melt pool via powder nozzle and can easily fabricate a heterogeneous material with desired properties and characteristics via successive and simultaneous depositions of different materials [2], thus this technique has great potential in repairing worn parts, remanufacturing industry, and developing new materials like functionally graded materials. DED-L, using laser as the heat source, is widely used in aerospace, medical, energy and automotive applications due to high dimensional accuracy and low surface roughness [3].

Ni-based alloys have been widely used in the aerospace industry due to their high strengths at elevated temperature [4]. Many of the Ni-based components are in highly complex shapes that are very expensive to produce using conventional machining [5] and DED has great advantage over fabricating intricate parts. Thus, typical weldable Ni-based alloys such as Inconel 625 and Inconel 718 have been used as feedstock materials in DED for a long time. Commercially produced IN718 powder was used as the feedstock materials for DED technology in [6] and it was found that the deposit exhibited strongly anisotropic properties, which can be reduced significantly by subsequent hot isostatically pressing (HIP) operation. A series DED deposited IN625 samples have been successfully fabricated in [7] and the possibility of manufacturing/repairing directionally

* Corresponding authors at: Institute of Mechanics, Chinese Academy of Sciences, Beijing 100190, China
E-mail addresses: xlhe@imech.ac.cn (X. He), tianchongxin@imech.ac.cn (C. Tian).

https://doi.org/10.1016/j.jallcom.2021.162976
0925-8388/

solidified components by DED when following appropriate processing strategy was demonstrated.

In metal additive manufacturing, application of a direct energy source, such as a laser or electron beam to melt alloy powders locally results in higher temperature gradient than conventional manufacturing processes. The high temperature gradient in AM leads to the grain structure of deposited components favoring epitaxial growth from previously deposited layers thus, resulting in anisotropy of mechanical properties of metallic AM components [8–10]. Many efforts have been made to control crystal growth in AM, which fall into two categories (post-processing treatments like heat treatment are not considered here because the focus of this work is crystal growth of as-deposited parts): (a)modifying the chemistry of the alloy composition to control the nucleation and/or (b) controlling the processing conditions during solidification. By adding nucleation agents, components with fully equiaxed crystals can be produced in AM. Zr nanoparticles were added to Al7075 powder and fully equiaxed component was produced using selective laser melting (SLM) [11], producing crack-free materials with strength double that of the most common additively manufactured aluminum alloy. An alloy containing grain refining solutes (Ti-3Al-8V-6Cr-4Mo-4Zr) and thermodynamically stable nucleant particles (La_2O_3) was used as feedstock materials for wire + arc additive manufacturing process (WAAM) in [12]. Grain refinement and equiaxed grain formation were achieved attributed to β-Ti nucleation on La_2O_3 when proper processing parameters were applied to decrease temperature gradient sufficiently to permit constitutional supercooling. The possibility of interfering with the columnar growth by adding nanoparticles is demonstrated numerically in DED [13]. By addition of La_2O_3, the heterogenous nucleation was promoted in DEDed NiTi alloy [14]. In general, adding inoculants with known undercooling promotes the equiaxed grain growth due to the promotion of nucleation events [15–17]. However, not all alloys can find their suitable nucleating agents. Lattice matching is needed to determine the particulate compositions and crystallographic faces with the highest probability of inducing epitaxial, heterogeneous nucleation [11] and a software is developed with Citrine Informatics that uses lattice matching algorithms to search through crystallographic databases for the highest matching crystal structures. Despite this software, so far, it is still hard to find potential nucleation agents. Even though suitable nucleation particle is found, atomization of additive feedstock is difficult and expensive [18].

Other researchers have attempted to control crystal growth mainly by changing processing conditions. Through changes in scan strategy between point and line, highly misoriented micro scale grains grew upon primarily columnar oriented grains in electron beam additive manufacturing (EBAM) [19]. With the increase of scanning speed, less equiaxed zone was obtained in SLM of IN625 [20]. In laser surface re-melting of directionally solidified nickel-based superalloys, the occurrence of stray grain region could be effectively controlled by reducing the heat input [21]. It is shown in [22] that the decrease of energy density could lead to columnar to equiaxed transition (CET) in laser melting deposited V-5Cr-5Ti alloys. As demonstrated by a well-tested multiscale phase-field model considering heterogeneous nucleation, grain selection and grain epitaxial growth, the increase of scanning speed and preheating temperature promotes the CET because of the increase of undercooling [23]. In pulsed diode laser-deposited of Waspaloy, it is found that long cycle periods and short pulse lengths could result in a highly columnar microstructures due to the elongation of melt pool and consequently a reduction in solidification front angle [24]. Also, in quasi-continuous-wave laser powder deposition process, the periodic push-and-pull motion of solidification interface caused by the pulsed laser promotes the crystallographic orientation dispersion of columnar dendrites [25]. Samples with fine, equiaxed prior-β grains were manufactured in DED with high-intensity ultrasound [26].

However, efforts trying to modulate crystal growth by varying processing conditions have little effects on crystal growth pattern and texture randomization especially in DED where the variation of melt pool size mainly influences the relative sizes of columnar-equiaxed growth regions due to the relatively small change of melt pool morphology [27]. More significant variation of microstructure has been achieved in selective laser melting (SLM) and welding under conduction and keyhole modes resulted from high power density and small molten pool in these two techniques. The preferential crystal growth direction under the conduction mode is closer to ⟨001⟩ direction while the crystal grains orientation under the keyhole mode tends to be ⟨001⟩ and ⟨101⟩ direction [28]. Texture transition from a strong {110}⟨001⟩ Goss texture along the laser scanning direction to a weaker {110}⟨001⟩ Goss texture in addition to a ⟨100⟩ fiber texture parallel to the scanning direction was achieved by changing the relative position between shielding gas flow direction and scanning direction in SLM [29]. This was assumed to be caused by melt pool shape change possibly due to local attenuation of the effective laser power density transmitted to the powder bed. Melt pool variation has been achieved by laser beam shaping in SLM and longitudinal elliptical beam shape resulted in the stronger texture for the columnar regions than circular Gaussian and transverse elliptical beam shape due to the generation of melt pool with shorter, wider and shallower dimension [30]. Crystal growth under different melt pool morphology by changing welding speed was investigated both experimentally and numerically during keyhole mode laser welding [31,32]. With the decrease of welding speed, coarser grain and larger axial columnar grain region were found in the weld. In DED, compared with SLM, the relatively small change of melt pool morphology such as depth/width ratio is due to the low power density and has little impact on the growth direction of columnar crystals. It is uncommon to increase power density like SLM because the spot diameter used in DED (~mm) is often two orders of magnitude larger than that in SLM (~10 μm).

In this work, in order to achieve high power density in DED, experiments were conducted under the spot diameter of 1 mm. Experiments under relatively low power density with spot diameter of 2 mm were also conducted to elucidate the effect of power density on crystal growth. The aim of this work is to describe further the different crystal growth pattern under different melt pool morphology of Ni-based superalloys samples fabricated by DED-L and explain how melt pool morphology combined with solidification parameters affects the microstructure of a material. In this paper, single scan tracks of Ni-based superalloys under different power density were fabricated on 304SS substrate. Optical microscope and Electron backscattered diffraction were then used to characterize melt pool and crystal growth. Further analysis about process, melt pool morphology, crystal structure and size were conducted.

Table 1
Chemical composition of 304SS substrate and Ni45 powder (wt%).

	Fe	Ni	Cr	C	Mn	P	Si	S
304SS (substrate)	Bal.	8.0–10.5	18–20	≤0.080	≤2.0	≤0.045	≤1.0	≤0.030
Ni45 (powder)	17.0	Bal.	14.0	0.4	–	–	3.0	–

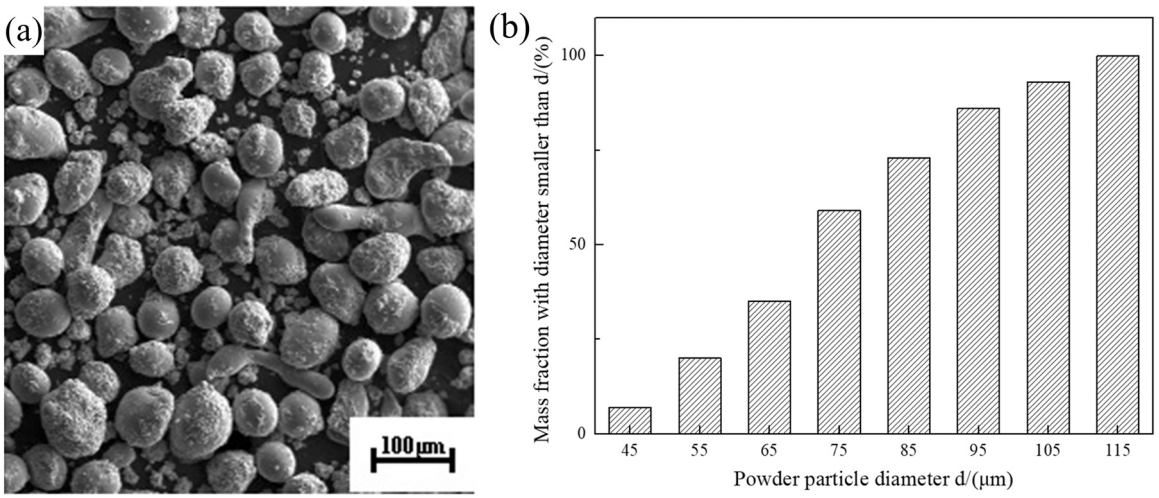

Fig. 1. (a)The SEM image for Ni45 powder particles and (b)the particle distribution of powder materials.

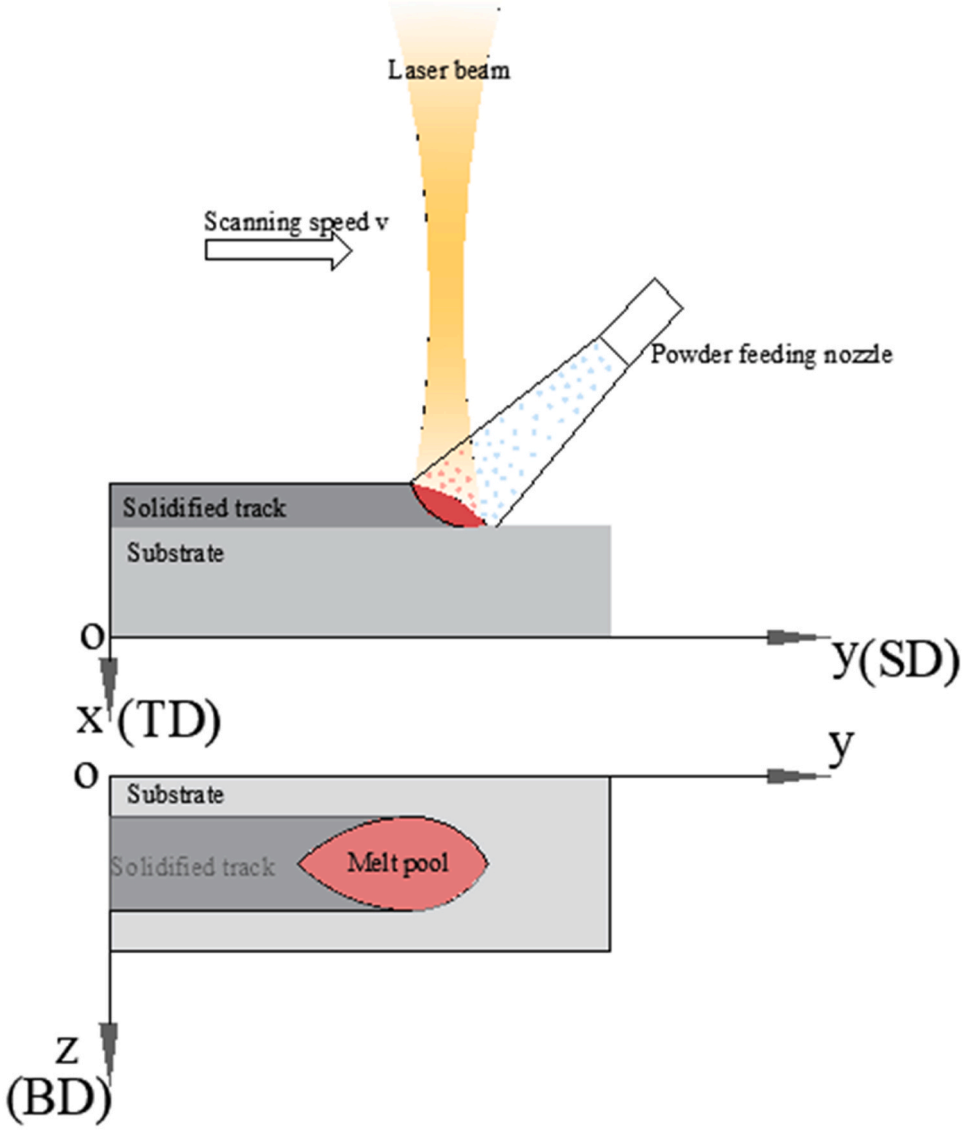

Fig. 2. Schematic representation of DED-L.

Table 2
Processing parameters used in DED-L.

Sample label	Laser power P/ (W)	Spot diameter d/ (mm)	Scanning speed (mm/s)	Powder feeding rate (g/min)	Power density (W/mm^2)
A	300	2	2	14.0	24
B	500	2	2	14.0	40
C	700	1	8	11.7	223

2. Experimental setups

2.1. Materials and fabrication method

The powder material used for the study was Ni45, with composition and particle distribution shown in Table 1 and Fig. 1(b), respectively. Fig. 1(a) is the scanning electron microscope (SEM) photograph of powder particles, showing mostly spherical morphology. The substrate material was polycrystalline 304 stainless steel, with the composition shown in Table 1. The substrate was mounted to make the roughness below 0.8 μm and washed by acetone before experiment.

The DED samples were manufactured using a self-developed five-axis gantry robot system equipped with Trumpf Nd+: YAG laser and DPSF-2 powder feeding machine. A schematic diagram of DED-L process is shown in Fig. 2. In DED-L, laser was used as the heat source and powder particles were fed laterally into the melt pool by inert gas such as argon. The laser and powder feeding nozzle synchronously moved along the predefined scanning strategies. With the solidification of melt pool, scan tracks formed over the substrate. The laser wavelength was 1030 nm and the focal length was 160 mm. The laser spot diameters (d) were set to be 1 mm with a defocus of 4.96 mm and 2 mm with a defocus of 9.98 mm. The powder was carried by argon (99.99%~99.999% purity) and the gas flow rate was set at 5.8 L/min, with a powder flow diameter of 4 mm and an inclination angle of 50°. Specific processing parameters and sample labels are shown in Table 2 and power density is defined as $4P/(\pi d^2)$.

2.2. Sample preparation and characterization

The samples were wire-cut from the substrate using a wire electrical discharge machine. Then, all the samples were mounted and ground using 60#, 200#, 600#, 1000# and 1500# silica sandpaper in order. Polishing was carried out using cloths with 2 μm diamond suspension. In order to display the microstructure under Optical Microscope (OM), the samples were electrically etched in 5 ml H_2SO_4 + 95 ml C_2H_5OH solution under the voltage of 20.0 V for 5 s. The samples were observed on a MD-50 UM200i optical microscope.

After rough grinding and polishing, samples were polished using 0.25 μm colloidal silica suspension for electron backscattered diffraction (EBSD) experiments. The EBSD characterization was carried out on a QUANTA FEG 450 scanning electron microscope equipped with EDAX system. The acceleration voltage of the SEM during acquisition was 20 kV. Post processing of the collected data was conducted using TSL OIM v7 software.

3. Results

3.1. Melt pool shapes and dimensions

Different melt pool shapes under different power density are displayed in Fig. 3. According to Fig. 3, the melt pool dimensions are measured and displayed in Fig. 4.

For the same spot size (Sample A and B, spot size = 2 mm), the height and width of melt pool increase with the increase of power density (sample A: 24 W/mm^2, sample B: 40 W/mm^2). Comparing sample C (spot size = 1 mm) with sample B (spot size = 2 mm), the width decreases although the power density increases nearly five times (from 40 W/mm^2 to 223 W/mm^2), meaning that the melt pool width is mainly determined by spot size. The height of melt pool slightly increases from sample B and C. As for the ratio of depth against width (aspect ratio), the ratio increases with the increase of power density. Sample A processed under low power density was

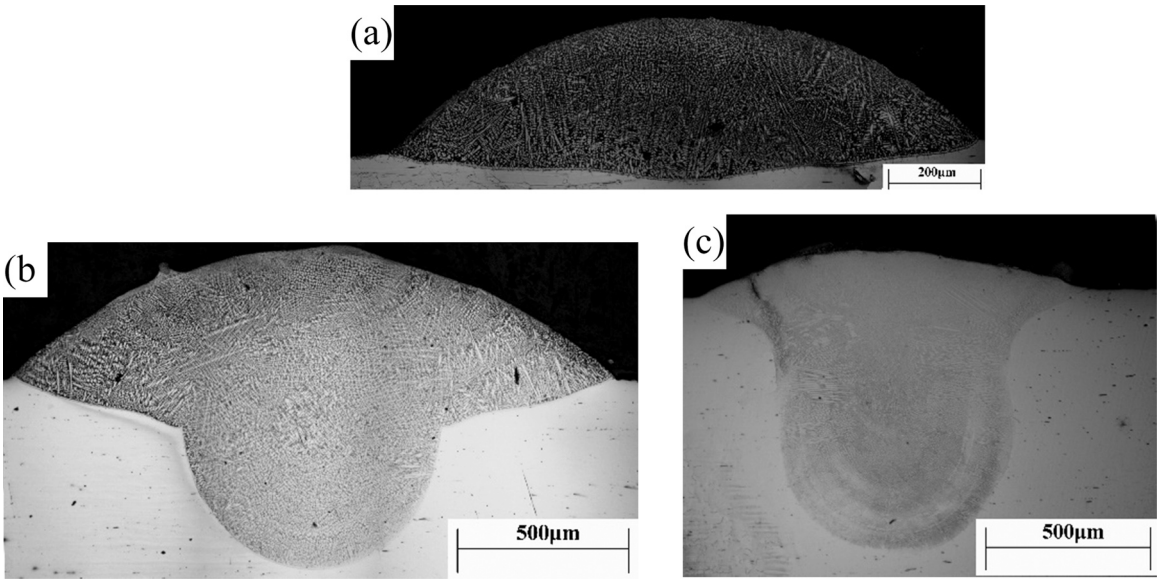

Fig. 3. OM images of melt pool for (a)Sample A, (b)Sample B and (c)Sample C.

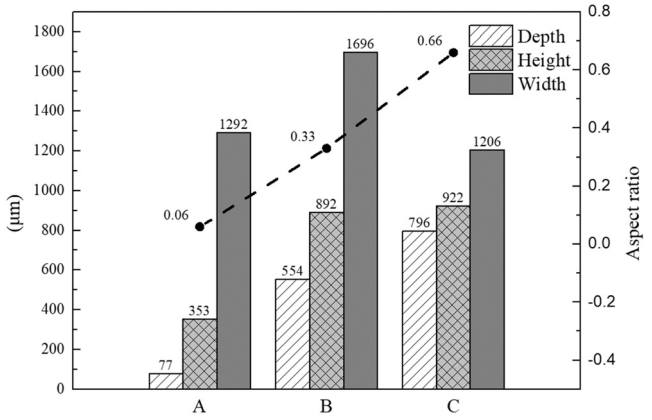

Fig. 4. The melt pool dimensions (height, width, depth and aspect ratio) for all three samples.

shown to exhibit wide and shallow spindle-like melt pool. With the increase of power density, sample B prepared under relatively higher power density was shown to exhibit wider and deeper melt pool with two sharp turning points/steps. Melt pool manufactured under higher power density (Sample C) became narrower with high aspect ratio.

3.2. Crystal growth patterns under different melt pool morphology

3.2.1. Melt pool with low aspect ratio (Sample A)

In order to investigate the effect of melt pool morphology on the microstructure, EBSD experiments were conducted on the transverse (xz plane in Fig. 2), horizontal (yz plane in Fig. 2) and central longitudinal (xy plane in Fig. 2) planes for samples A, B and C. Fig. 5 shows Inverse pole figures (IPFs) for the transverse, central longitudinal and horizontal cross sections of single scan track deposited under relative low power density of 24 W/mm^2 (Sample A), with the three-dimensional (3D) visualization of the grain structures illustrated in Fig. 5(d). The melt pool boundary was highlighted in black thick solid line for more clarity. The relationship between colors in IPFs and crystal orientations is shown in Fig. 5(d), within the direction illustrated in Fig. 2. As shown in Fig. 5(a), there are clearly two different grain structure regions. In region II, columnar crystal grains grew perpendicularly to the relatively flat boundary of melt pool and the reddish color indicated strong epitaxy along (001) direction. In region I, nearly equiaxed crystal grains with random orientations grew at the top of the melt pool, surrounding the columnar crystal grains. These crystal evolution patterns were also verified in the central longitudinal section (Fig. 5(b)) while columnar crystal grains, showing strong (001) orientations, grew nearly perpendicularly to the substrate and were truncated by the equiaxed crystal grains with random orientations at the upper part. In this plane, it is also worth mentioning that the columnar crystals grew with a slight inclination towards the scanning direction. As for the horizontal section (Fig. 5(c)), since this section was sampled 100 μm away from the top surface, the equiaxed crystal grains were somewhat cleared, thus only the horizontal projection of epitaxial columnar grains was shown. As shown in this picture, columnar crystals growing along (001) direction showed nearly equiaxed shape in the top view. Overall, the 3D visualization shown in Fig. 5(d) indicated strong epitaxy along (001) direction.

In order to further study the difference between two regions obtained in Sample A, quantitative comparison of the transverse

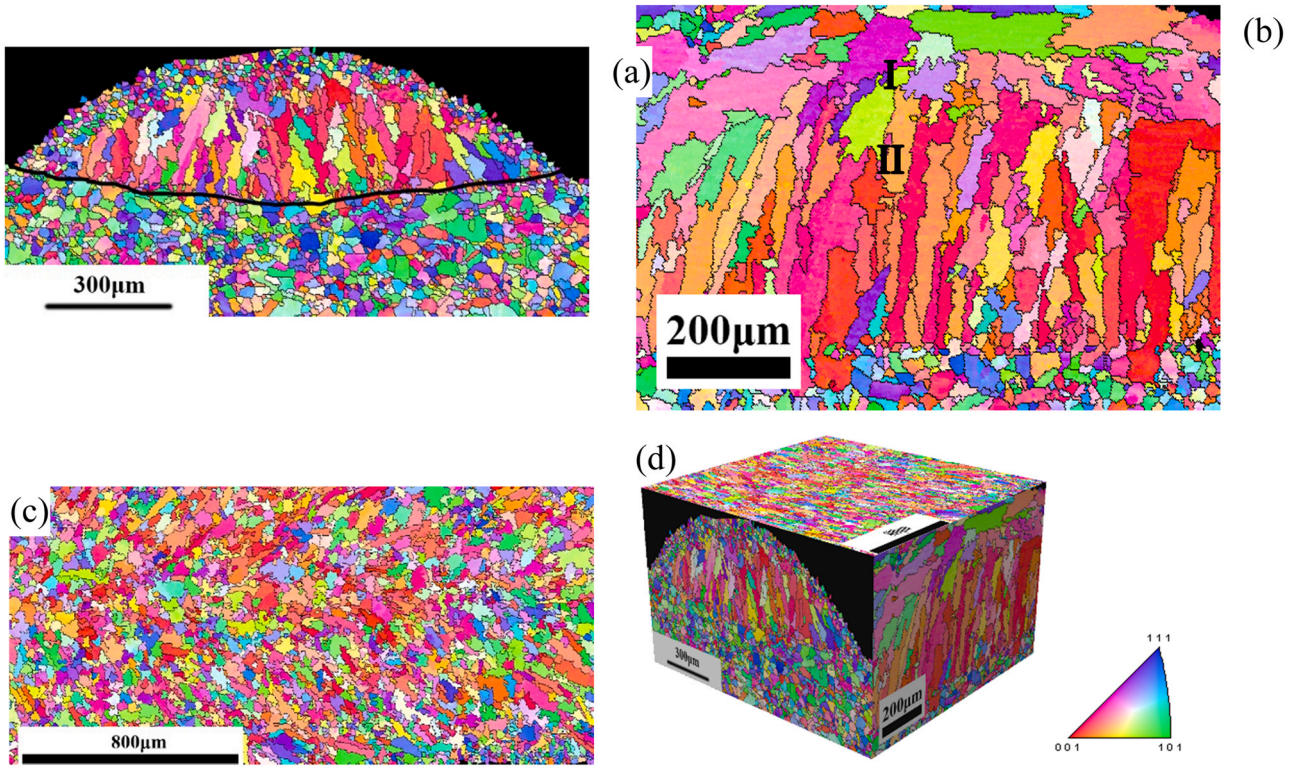

Fig. 5. Inverse pole figures superimposed by grain boundary for sample A (a) transverse plane, (b)central longitudinal plane, (c)horizontal plane 100 μm away from the top surface and (d) 3D visualization.

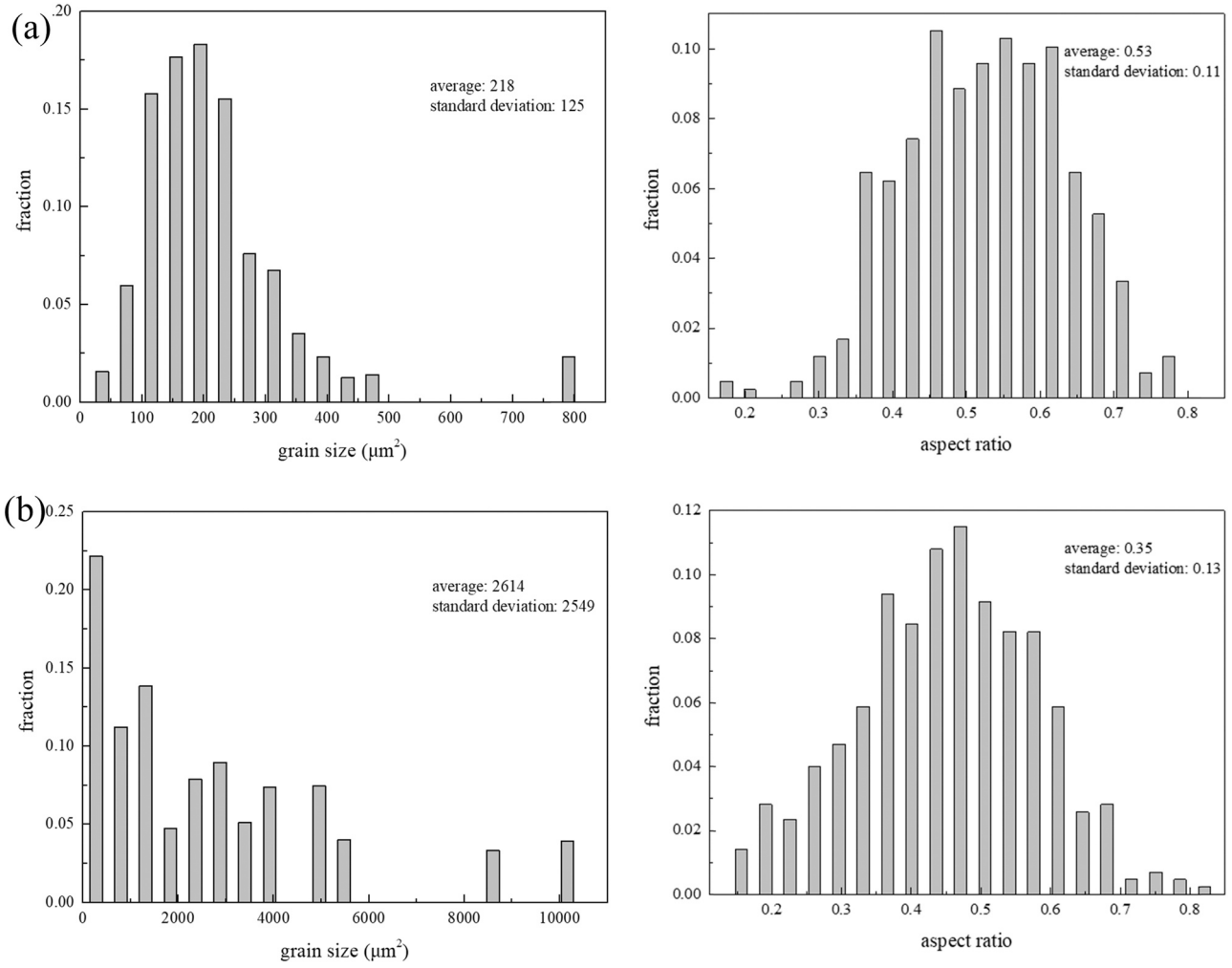

Fig. 6. Comparison of grain size and aspect ratio in (a) Region I and (b)II corresponding to Fig. 5(a).

section including grain size and aspect ratio were shown in Fig. 6. Due to the differences in defining size for columnar and equiaxed crystals, occupied area is used here to demonstrate the grain size. For a single crystal, the ratio of shortest distance to the longest distance is taken as aspect ratio. As shown in Fig. 6, grain size in Region II with the average size of 2614 μm^2 is much larger than in Region I with the average size of 218 μm^2. The aspect ratio of Region II is smaller than that of Region I, meaning more elliptical columnar crystals in Region II.

3.2.2. Melt pool with high aspect ratio

As for sample C prepared under high power density, with IPFs shown in Fig. 7, columnar crystal grains grew perpendicularly to the contour of melt pool, separating melt pool into four regions according to the crystal growth direction. At region I, nearly-equiaxed grains were found, with random grain orientations. At region II, the crystal grains grew horizontally where the boundary of melt pool was nearly perpendicular. Also, the crystal growth pattern was almost symmetrical along the center line of melt pool. Orientation here tended to be ⟨110⟩ judging from the greenish color in this region. At region IV, columnar grains grew approximately vertical to the boundary of melt pool. However, since the melt pool boundary in this region has an inclination angle to the substrate, crystals here grew at an angle along the scanning direction which was clearly shown in the central longitudinal section. At region III, columnar grains grew perpendicularly to the boundary colliding with each other and nearly perpendicular columnar crystal grew. This growth mode has been verified in the IPF of horizontal section (Fig. 7(c)). Long axial columnar grains were observed in the middle of scan track where inclined crystals were shown bilaterally. However, though the longitudinal section was sampled at the central of single scan track, the axial columnar crystal in Region III was not clearly shown in Fig. 7(b) due to the sampling error and subsequent material removement such as grinding and polishing necessary for further EBSD characterization.

The orientation of columnar crystals in different regions was different as stated above, but quantitative characterization about it was not applicable due to the little sampling points in each individual region. However, other than orientation, the aspect ratio and average length also varied in different regions. It should be noted that the columnar crystals vary with the sampling and observation planes. The grain size and aspect ratio shown in Fig. 8 are just phenomenological. As shown in Fig. 8(b), the grain size in Region II is largest.

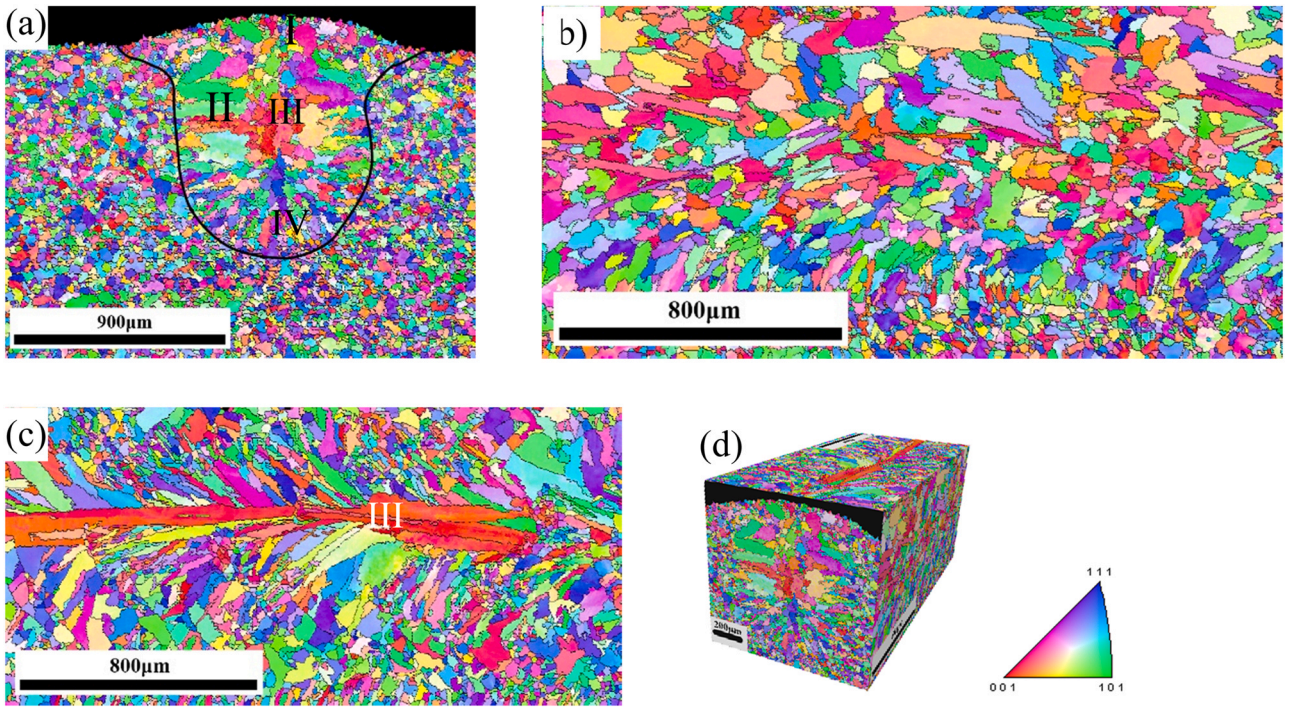

Fig. 7. IPFs superimposed by grain boundary for sample C (a) transverse section, (b)central longitudinal section, (c)horizontal section and (d) 3D visualization.

3.2.3. Melt pool with medium aspect ratio

IPFs for sample B is presented in Fig. 9. It can be observed from Fig. 9(c) that the horizontal plane was composed of columnar grains with an inclination towards scanning direction. When observing the grain structure in the transverse and central longitudinal plane, the columnar grains had similar appearances to equiaxed grains, which might be misleading. Whereas, this seemingly misleading appearance further verified the uniformity of columnar grains observed in the horizontal plane (columnar morphology can also be verified through the grain structure revealed in the transverse (Fig. 9(a)) and central longitudinal (Fig. 9(b)) planes). Remarkably, this is the meaning of 3D visualization of grain structure and investigating from three dimension. Generally speaking, for Sample B, columnar grains grew with an inclination angle converged in the center of scan track. At the middle of scan track, unlike the long axial columnar crystal observed in sample C, the majority of columnar crystals on both sides converge here with several discontinuous columnar grains. The orientations of these discontinuous crystals are shown to be parallel to the scanning direction since they are mostly reddish. It can be observed from the transverse section (Fig. 9(a)) and longitudinal section (Fig. 9(b)) of sample B that there is not a dominant direction for crystal growth. Although there is a sharp turning of the melt pool boundary, no obvious change of crystal growth is observed.

3.3. Effect of power density on crystal growth

As analyzed above, crystal growth with significantly different appearances has been demonstrated under different power density. In order to quantify the effect of power density on crystal growth evolution, texture, aspect ratio and grain size have been studied. Fig. 10 shows the pole figures (PFs) under various power density. It should be noted that following analysis is based on sampled taken from transverse section unless specified additionally. The preferred crystallographic orientation is (100) for sample A and (110) for sample B and C. The texture density is the smallest for sample C while the power density is highest in this work. Orientation distribution function (ODF) using Roe Euler angles is shown in Fig. 11. In order to convert Euler angles (ψ, θ, φ) to Miller indices $\{hkl\}(uvw)$ for cubic system, calculation was based on the following formulas [33].

$$h : k : l = (-sin\theta cos\varphi):(sin\theta sin\varphi): cos\theta$$

$$u : v : w = (cos\psi cos\theta cos\varphi - sin\psi sin\varphi):(-cos\psi cos\theta sin\varphi - sin\psi cos\varphi) :(cos\psi sin\theta)$$

The maximum texture indexes of three samples studied are (001)[−110] 7.7 × random (Fig. 11(a)) for sample A, (101)[010] 8.1 × random (Fig. 11(b)) for sample B and (101)[− 101] 5.1 × random (Fig. 11(c)) for sample C. It can be concluded that the texture intensity decreased with the increase of power density in this work.

The grain size and aspect ratio distribution for the three samples studied are shown in Fig. 12. Generally, grain size for sample B and C were much larger than sample A. Under the same spot diameter, with the increase of power density, the grain size increases from 2173 μm^2 (Sample A) to 7804 μm^2 (Sample B). Whereas grain size of Sample C (4135 μm^2) was smaller than that of sample B despite the increased power density due to different spot diameter. Meanwhile, Sample A exhibits the smallest aspect ratio which means that crystals in this sample are more elliptical. Despite the dramatic change in

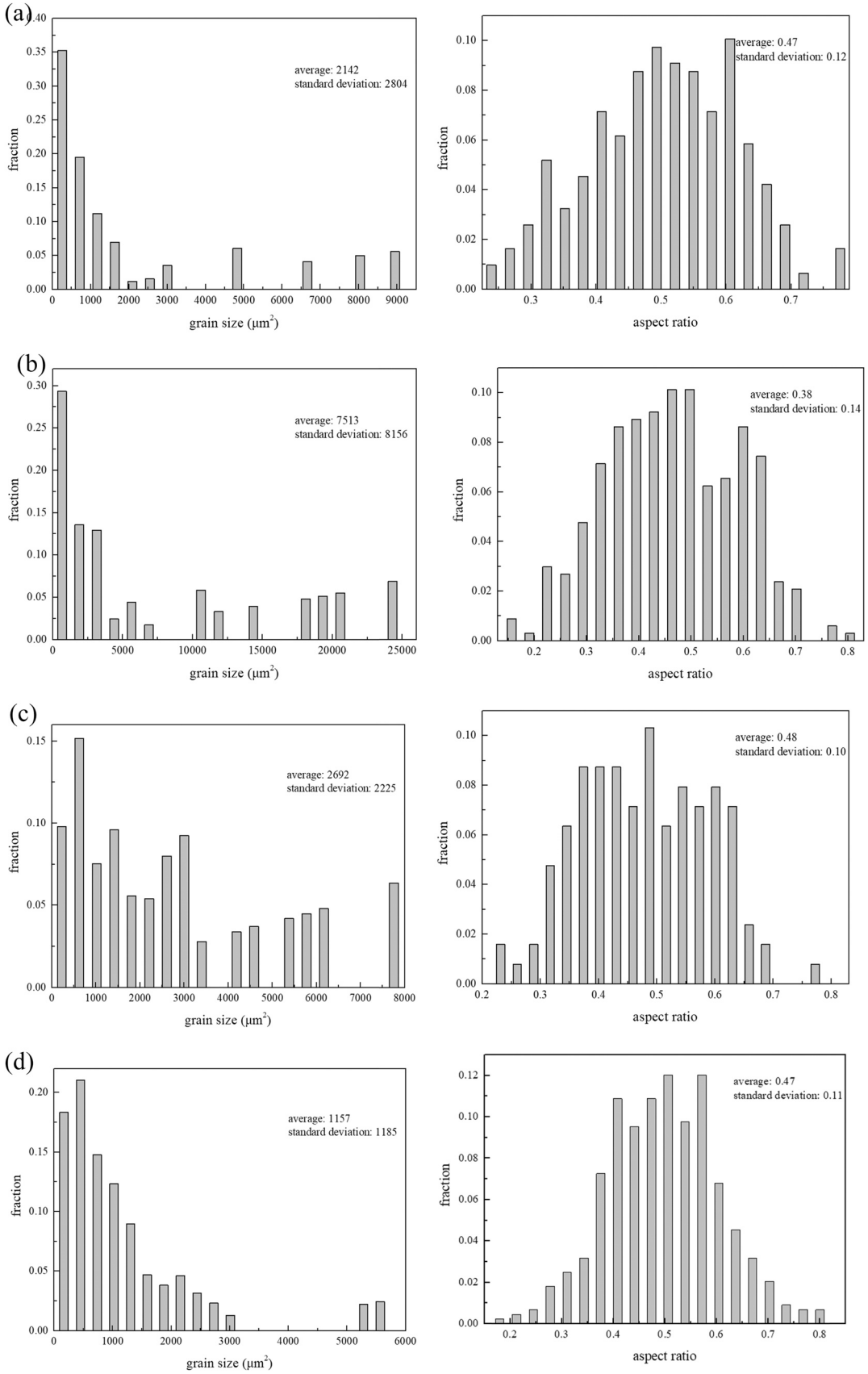

Fig. 8. Comparison of grain size and aspect ratio in (a) Region I, (b) II, (c) III and (d) IV corresponding to Fig. 7(a).

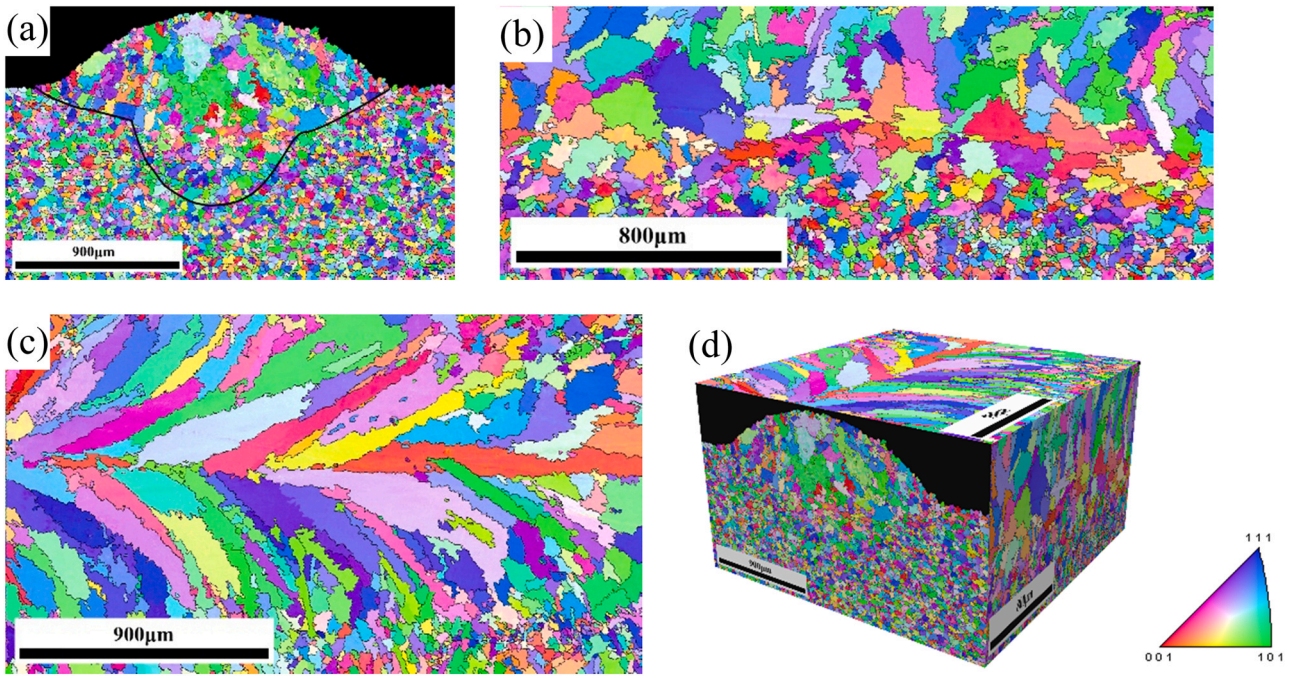

Fig. 9. IPFs superimposed by grain boundary for sample B (a) transverse section, (b)central longitudinal section, (c)horizontal section and (d) 3D visualization.

power density, all three samples exhibit similar distribution of grain size and aspect ratio.

4. Discussion

Essentially, mechanical behaviors and performances of additively manufactured components, which have always raised great concern since the arise of this technique, are determined by microstructural development and texture evolution. However, there is no efficient and precise way of controlling crystal growth especially site-specifically. Efforts trying to modulate crystal growth by varying processing conditions have little effects on crystal growth pattern and texture randomization especially in DED. Here, this work tries to explore the possibility of diverse crystal growth pattern in DED-L by controlling spot diameter and power density. The mechanism behind it is discussed below.

This work has shown that considerable control over the crystal grain growth and texture can be achieved by changing the melt pool morphology , including the change of melt pool shape and solidification parameters at the liquid/solid interface. The melt pool boundary, representing the liquid-solid interface, is essential for crystal growth. On the one hand, the driving force of grain growth is maximum along the direction of local maximum heat flow direction, which is perpendicular to the melt pool boundary. On the other hand, grain morphology and grain size are determined by the solidification parameters (morphology factor, G/R and cooling rate, CR) at liquid-solid interface, which is demonstrated as melt pool boundary in the experimental observations afterwards.

Three crystal growth patterns are obtained by varying power density. At low power density, growth pattern in Fig. 5 is obtained. As shown in the transverse section (Fig. 5(a)), under low power density, shallow melt pool with relatively small aspect ratio was achieved due to the low penetration depth of heat. Since the substrate was composed of polycrystalline crystal stainless steel grain, as illustrate in Fig. 13, columnar crystals grew from it with no preferred orientation to substrate crystal lattices and grew along the direction of maximum heat flow, which was perpendicular to the melt pool boundary. Thus, at the lower part of melt pool, columnar crystal grew along < 001 > direction as shown in Fig. 13(a) and 13(b). However, at the upper part of the melt pool, due to the inclination of melt pool boundary and the change of thermodynamic condition, solidification parameter, which is the morphology factor (G/R), here decreased below the critical columnar-to-equiaxed transition G/R number, causing the crystal here to exist as equiaxed crystals. Similar result has been studied in [34]. In this paper, a three-dimensional numerical model considering Marangoni convection, phase change, heat conduction has been developed to simulate temperature field which is then used to calculate solidification parameters. The G/R increases approximately from 1000Ks/mm^2 to 2998Ks/mm^2 from the bottom to the top of melt pool. At the central longitudinal section, the trailing edge of melt pool was in a curved shape, causing the columnar crystals to grow slightly inclined towards scanning direction as shown clearly in Fig. 5(b) and the inclination angle was approximately 15°.

Under high power density, crystal growth pattern was separated into four regions. As shown in Fig. 14, at Region II (middle upper part of the melt pool), the direction of columnar grains growth was nearly parallel to y-axis because the melt pool boundary here was almost vertical. At Region IV (lower part of the melt pool), columnar crystal grains grew with inclined grains. This is because the melt pool boundary in this region is inclined gradually in a curved shape from the nearly straight shape in upper Region II. As for equiaxed crystals with random orientation in Region I, this is mainly because of the small G/R here. The axial columnar grew in Region III, which is

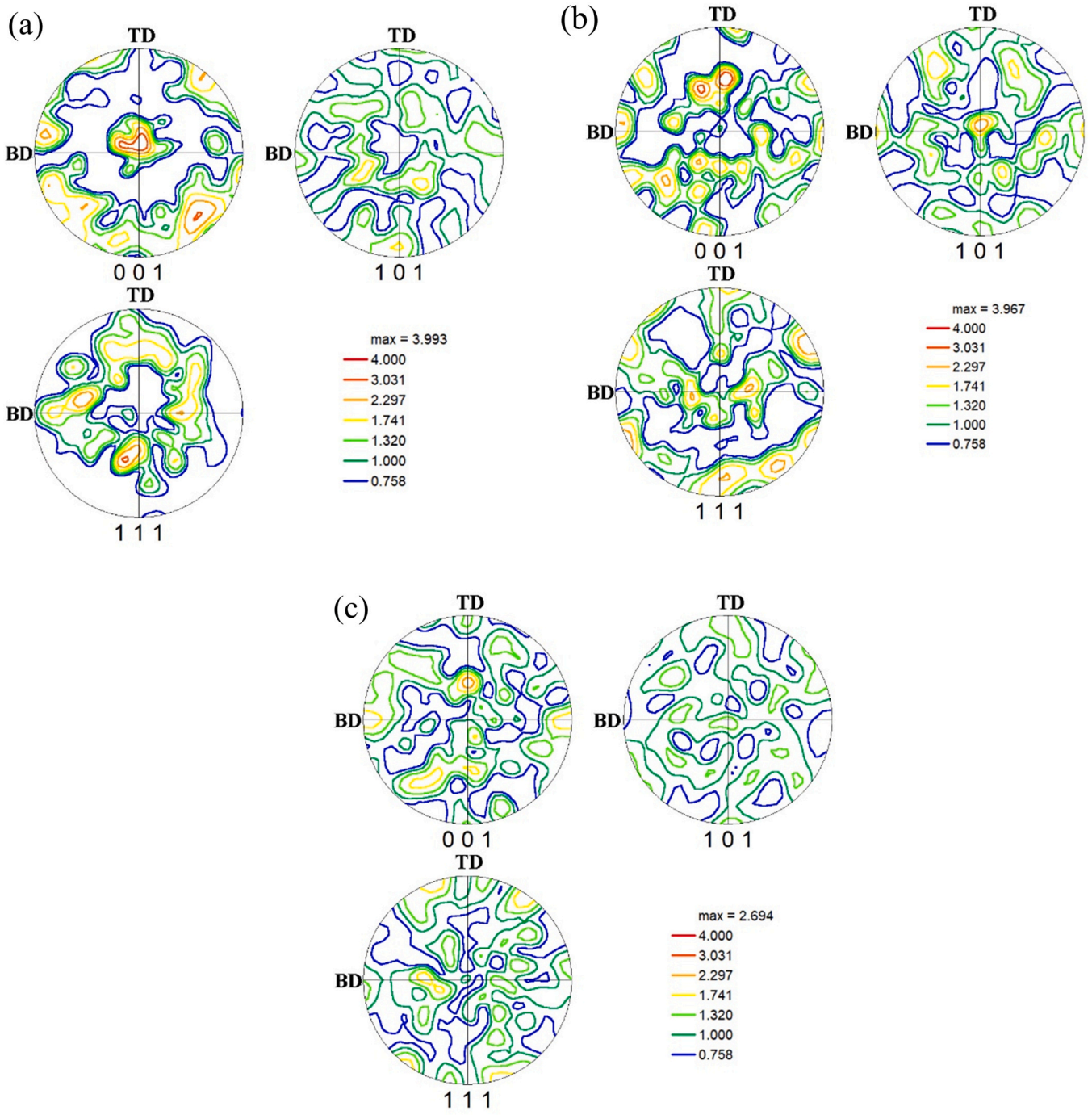

Fig. 10. Stereographic {001}, {101} and {111} pole figures for sample (a) A, (b) B and (c) C.

due to the collective effect of collision of columnar growth in Region IV and the curved melt pool boundary. Also, G/R here was large which had promoted the epitaxial columnar growth.

Growth pattern of inclined columnar grains with several central axial columnar grains was achieved under the power density of 40 W/mm^2 (Sample B). The columnar crystals grew perpendicular to the melt pool boundary on both sides and collided with each other, promoting the central axial columnar crystals. Schematic crystal growth of this sample is shown in Fig. 15. Inclined columnar crystals grew due to the curve melt pool boundary. And the central discontinuous axial columnar grains grew due to the collective effects of collision of bilateral columnar crystals and large G/R here.

With the increase of power density, average grain size increases from 2173 μm^2 (Sample A) to 7805 μm^2 (Sample B) under the same

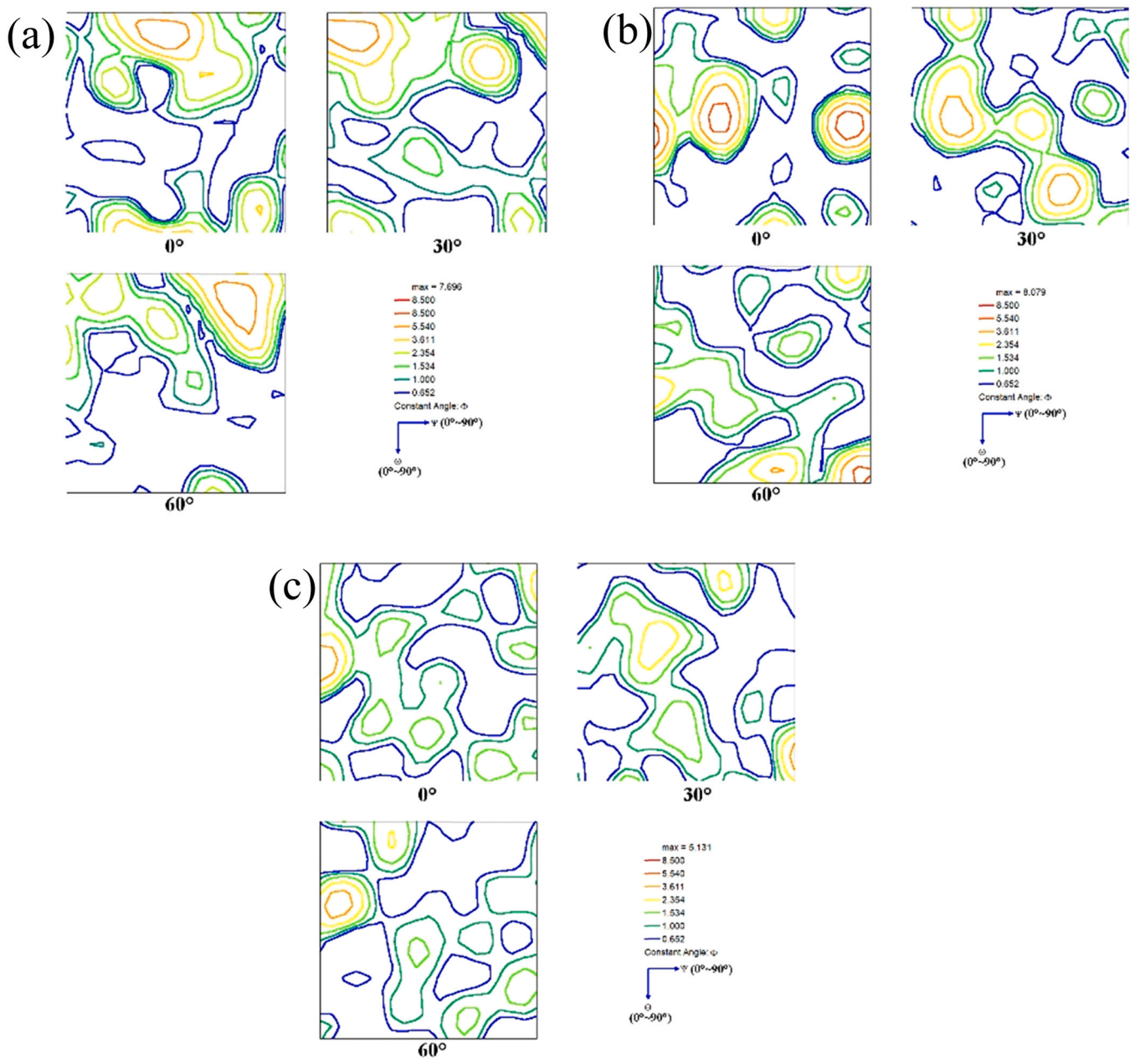

Fig. 11. ODF sections with φ = 0°, 30° and 60° for sample (a) A, (b) B and (c) C, respectively.

spot diameter (Fig. 12(a, b)). Similar results are shown in [35,36] and it is confirmed to be linked to the decrease of cooling rate (CR) with the increase of power density.

When it comes to applications involving multidirectional stresses, the anisotropy of mechanical behaviors, which originates from columnar grains in AM, is detrimental [8,9]. When it comes to applications involving unidirectional stresses, microstructure with preferred orientation inclined with stress direction is favored such as single-crystal blade [37]. It is necessary to control crystal growth under specific working condition, accordingly. This work enriches the crystal growth pattern in DED-L and provides the possibility of controlling crystal growth by changing processing parameters. It is possible to get single crystal components under the crystal growth presented in Fig. 5. In order to weaken the anisotropy of mechanical behaviors, low texture density of crystal growth pattern in Fig. 7 is favored.

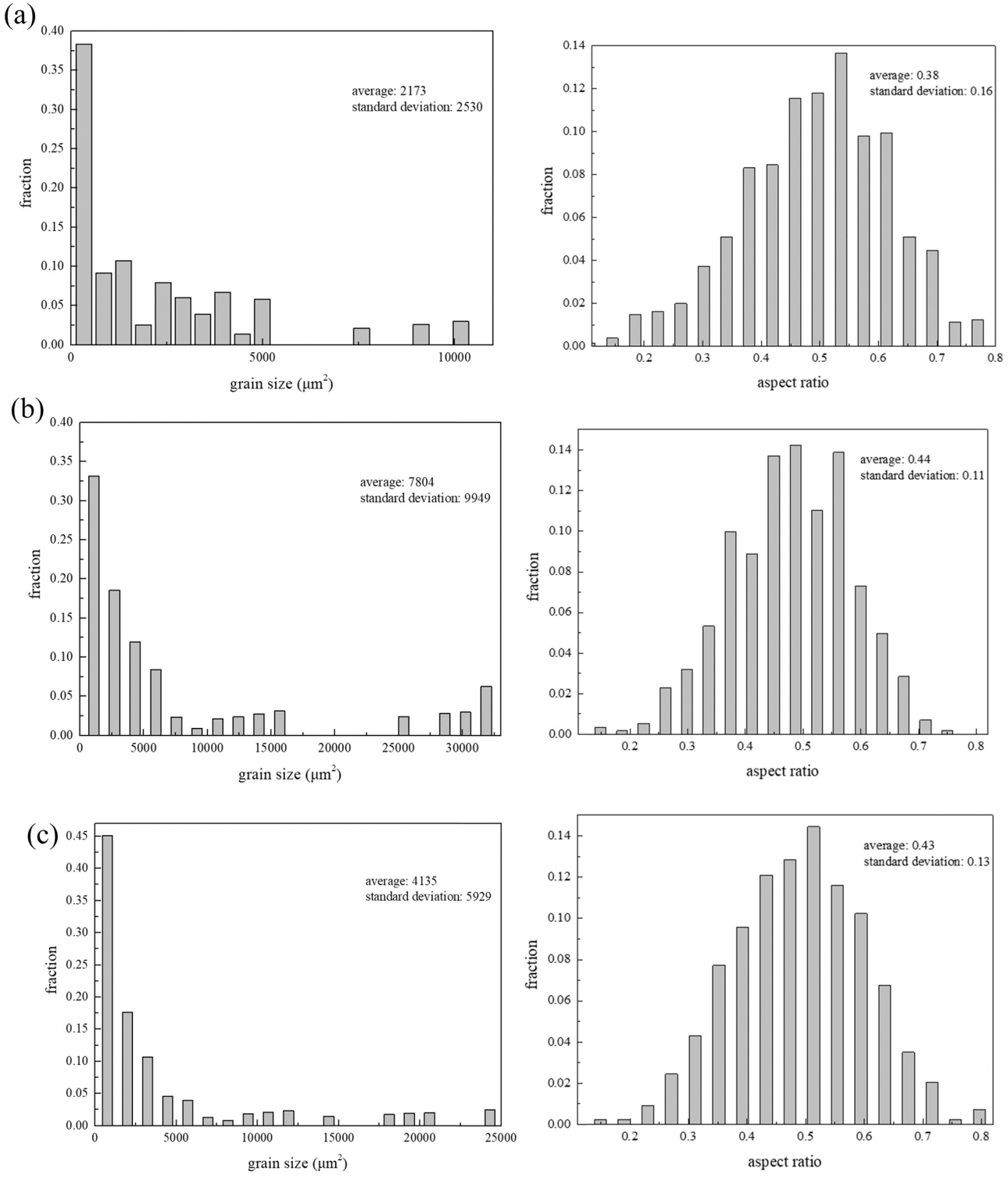

Fig. 12. Grain size and aspect ratio distribution for sample (a) A, (b) B and (c) C.

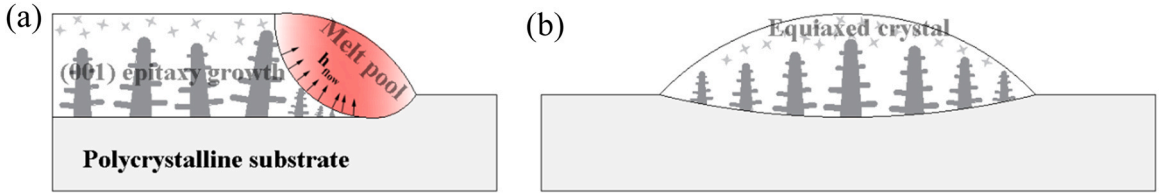

Fig. 13. Schematic diagram of crystal growth behaviors of (a) central longitudinal and (b) transverse section under shallow and wide melt pool for Sample A.

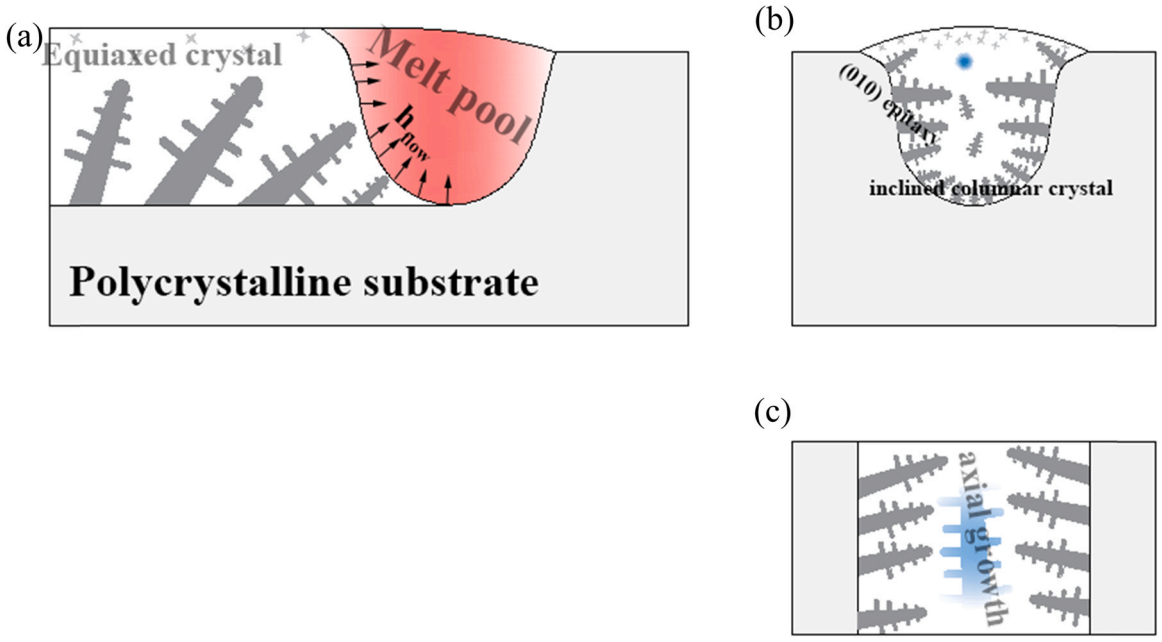

Fig. 14. Schematic diagram of crystal growth behaviors of (a) central longitudinal, (b) transverse and (c) horizontal section under deep and narrow melt pool with high aspect ratio for Sample C.

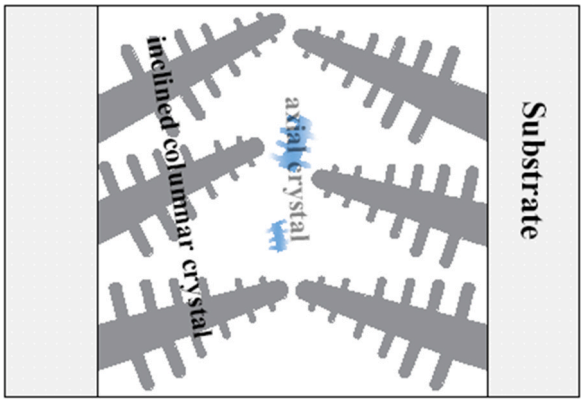

Fig. 15. Schematic diagram of crystal growth behaviors of horizontal section for Sample B.

5. Conclusion

Crystal growth has been a great concern in AM for a long time. In this paper, crystal growth pattern in DED of Ni-based superalloys have been modulated through control of melt pool morphology. Three dimensional EBSD characterization experiments were conducted to elucidate crystal growth evolution. Crystal structure appearance, texture, size and aspect ratio were studied. Relationship between power density, melt pool morphology, crystal structure was further illustrated. Main conclusions are as follows:

Under low power density of 24 W/mm^2, shallow and flat melt pool was obtained. Columnar crystal grains grew perpendicularly to the relatively flat boundary of melt pool and nearly equiaxed crystal grains with random orientations grew at the top of the melt pool.

Under high power density of 223 W/mm^2 with the spot diameter of 1 mm, deep and narrow melt pool shape was presented. Crystal growth pattern here was composed of four regions: nearly-equiaxed grains with random grain orientations at Region I; the horizontally symmetrically grown crystal grains at region II; axial columnar in the center at Region III; columnar grains grew approximately vertical to the boundary of melt pool at Region IV.

Under the power density of 40 W/mm^2, sample exhibited columnar grains with an inclination angle towards scanning direction and several discontinuous axial columnar at the center of scan track.

The diverse crystal growth patterns under the control of power density contributed to the melt pool morphology and solidification parameters at the solid-liquid interfaces. This work has demonstrated the feasibility of controlling crystal growth in DED-L by modulating melt pool morphology.

With the increase of power density, the preferred orientation transformed from (001) to (110) and the texture density decreased. The grain size increased with the increase of power density due to lower cooling rate. And the aspect ratio was the largest at the power density of 223 W/mm^2, meaning that more elliptical columnar grains grew.

CRediT authorship contribution statement

Jiayun Shao: Conceptualization, Methodology, Experiments, Manuscript, Investigation, Writing – original draft, Writing – review & editing. **Gang Yu:** Conceptualization, Experiment design. **Shaoxia Li:** Experiments, Writing – original draft. **Xiuli He:** Conceptualization, Writing, Supervision. **Chongxin Tian:** Experimental design, Supervision., Binxin Dong: Experiments, Writing - Review.

Declaration of Competing Interest

The authors declare that they have no known competing financial interests or personal relationships that could have appeared to influence the work reported in this paper.

Acknowledgement

This research did not receive any specific grant from funding agencies in the public, commercial, or not-for-profit sectors.

References

[1] T. DebRoy, H.L. Wei, J.S. Zuback, T. Mukherjee, J.W. Elmer, J.O. Milewski, A.M. Beese, A. Wilson-Heid, A. De, W. Zhang, Additive manufacturing of metallic

components - process, structure and properties, Prog. Mater. Sci. 92 (2018) 112–224.
[2] D.-G. Ahn, Directed energy deposition (DED) process: state of the art, Int. J. Precis Eng. Manuf. -Green. Technol. 8 (2) (2021) 703–742.
[3] D. Gu, X. Shi, R. Poprawe, D.L. Bourell, R. Setchi, J. Zhu, Material-structure-performance integrated laser-metal additive manufacturing, Science 372 (6545) (2021) 932.
[4] M.J. Donachie, S.J. Donchie, Superalloys: A Technical Guide, ASM International,, Materials Park (OH), 2002.
[5] J.J. Valencia, J. Spirko, R. Schmees, Superalloys 718, in: E.A. Loria (Ed.), 706 and Various Derivates, 625 TMS, Warrendale, PA, 1997, pp. 753–762.
[6] P.L. Blackwell, The mechanical and microstructural characteristics of laser-deposited IN718, J. Mater. Process. Technol. 170 (1–2) (2005) 240–246.
[7] G.P. Dinda, A.K. Dasgupta, J. Mazumder, Laser aided direct metal deposition of Inconel 625 superalloy: Microstructural evolution and thermal stability, Mater. Sci. Eng. A-Struct. Mater. Prop, Microstruct. Process. 509 (1–2) (2009) 98–104.
[8] J.J. Lewandowski, M. Seifi, Metal additive manufacturing: a review of mechanical properties, in: D.R. Clarke (Ed.), Ann. Rev. Mater. Res. Vol 46 2016, pp. 151–186.
[9] P.C. Collins, D.A. Brice, P. Samimi, I. Ghamarian, H.L. Fraser, Microstructural control of additively manufactured metallic materials, in: D.R. Clarke (Ed.), Ann. Rev. Mater. Res. Vol 46 2016, pp. 63–91.
[10] L.L. Parimi, G.A. Ravi, D. Clark, M.M. Attallah, Microstructural and texture development in direct laser fabricated IN718, Mater. Charact. 89 (2014) 102–111.
[11] J.H. Martin, B.D. Yahata, J.M. Hundley, J.A. Mayer, T.A. Schaedler, T.M. Pollock, 3D printing of high-strength aluminium alloys, Nature 549 (7672) (2017) 365.
[12] M.J. Bermingham, D.H. StJohn, J. Krynen, S. Tedman-Jones, M.S. Dargusch, Promoting the columnar to equiaxed transition and grain refinement of titanium alloys during additive manufacturing, Acta Mater. 168 (2019) 261–274.
[13] D.-R. Liu, S. Wang, W. Yan, Grain structure evolution in transition-mode melting in direct energy deposition, Mater. Des. 194 (2020).
[14] B. Lu, X. Cui, W. Ma, M. Dong, Y. Fang, X. Wen, G. Jin, D. Zeng, Promoting the heterogeneous nucleation and the functional properties of directed energy deposited NiTi alloy by addition of La_2O_3, Addit. Manuf. 33 (2020).
[15] M. Bermingham, D. StJohn, M. Easton, L. Yuan, M. Dargusch, Revealing the mechanisms of grain nucleation and formation during additive manufacturing, JOM 72 (3) (2020) 1065–1073.
[16] D.H. StJohn, M. Qian, M.A. Easton, P. Cao, The Interdependence Theory: The relationship between grain formation and nucleant selection, Acta Mater. 59 (12) (2011) 4907–4921.
[17] A. Prasad, L. Yuan, P. Lee, M. Patel, D. Qiu, M. Easton, D. StJohn, Towards understanding grain nucleation under additive manufacturing solidification conditions, Acta Mater. 195 (2020) 392–403.
[18] B.S. Murty, S.A. Kori, M. Chakraborty, Grain refinement of aluminium and its alloys by heterogeneous nucleation and alloying, Int. Mater. Rev. 47 (1) (2002) 3–29.
[19] R.R. Dehoff, M.M. Kirka, W.J. Sames, H. Bilheux, A.S. Tremsin, L.E. Lowe, S.S. Babu, Site specific control of crystallographic grain orientation through electron beam additive manufacturing, Mater. Sci. Technol. 31 (8) (2015) 931–938.
[20] L. Yuan, A.S. Sabau, D. StJohn, A. Prasad, P.D. Lee, Iop, Columnar-to-equiaxed transition in a laser scan for metal additive manufacturing, International Conference on Modelling of Casting, Welding and Advanced Solidification Processes2020.
[21] G. Liu, D. Du, K. Wang, Z. Pu, B. Chang, Epitaxial growth behavior and stray grains formation mechanism during laser surface re-melting of directionally solidified nickel-based superalloys, J. Alloy. Compd. 853 (2021).
[22] L. Bai, G. Le, X. Liu, J. Li, S. Xia, X. Li, Grain morphologies and microstructures of laser melting deposited V-5Cr-5Ti alloys, J. Alloy. Compd. 745 (2018) 716–724.
[23] P. Liu, Z. Wang, Y. Xiao, M.F. Horstemeyer, X. Cui, L. Chen, Insight into the mechanisms of columnar to equiaxed grain transition during metallic additive manufacturing, Addit. Manuf. 26 (2019) 22–29.
[24] R.J. Moat, A.J. Pinkerton, L. Li, P.J. Withers, M. Preuss, Crystallographic texture and microstructure of pulsed diode laser-deposited Waspaloy, Acta Mater. 57 (4) (2009) 1220–1229.
[25] Z. Liu, J. Shu, Effect of pulse frequency on the transport phenomena and crystal growth behavior in quasi-continuous-wave laser powder deposition of single-crystal superalloy, Metall. Mater. Trans. B-Proc. Metall. Mater. Proc. Sci. 51 (6) (2020) 2797–2810.
[26] C.J. Todaro, M.A. Easton, D. Qiu, D. Zhang, M.J. Bermingham, E.W. Lui, M. Brandt, D.H. StJohn, M. Qian, Grain structure control during metal 3D printing by high-intensity ultrasound, Nat. Commun. 11 (1) (2020).
[27] W.P. Liu, J.N. DuPont, Effects of melt-pool geometry on crystal growth and microstructure development in laser surface-melted superalloy single crystals, Math. Model. Single-Cryst. Growth a melt Pool. (Part I), Acta Mater. 52 (16) (2004) 4833–4847.
[28] H. Wang, L. Wang, R. Cui, B. Wang, L. Luo, Y. Su, Differences in microstructure and nano-hardness of selective laser melted Inconel 718 single tracks under various melting modes of molten pool, J. Mater. Res. Technol. -JMRT 9 (5) (2020) 10401–10410.
[29] O. Andreau, I. Koutiri, P. Peyre, J.-D. Penot, N. Saintier, E. Pessard, T. De Terris, C. Dupuy, T. Baudin, Texture control of 316L parts by modulation of the melt pool morphology in selective laser melting, J. Mater. Process. Technol. 264 (2019) 21–31.
[30] R. Shi, S.A. Khairallah, T.T. Roehling, T.W. Heo, J.T. McKeown, M.J. Matthews, Microstructural control in metal laser powder bed fusion additive manufacturing using laser beam shaping strategy, Acta Mater. 184 (2020) 284–305.
[31] H.L. Wei, J.W. Elmer, T. DebRoy, Crystal growth during keyhole mode laser welding, Acta Mater. 133 (2017) 10–20.
[32] L.-J. Zhang, G.-F. Zhang, J. Ning, X.-J. Zhang, J.-X. Zhang, Microstructure and properties of the laser butt welded 1.5-mm thick T2 copper joint achieved at high welding speed, Mater. Des. 88 (2015) 720–736.
[33] R.J. Roe, Description of crystalline orientation in polycrystalline materials 3. general solution to pole figure inversion, J. Appl. Phys. 36 (6) (1965) 2024-&.
[34] Z. Gan, G. Yu, X. He, S. Li, Numerical simulation of thermal behavior and multicomponent mass transfer in direct laser deposition of Co-base alloy on steel, Int. J. Heat. Mass Transf. 104 (2017) 28–38.
[35] A. Keshavarzkermani, E. Marzbanrad, R. Esmaeilizadeh, Y. Mahmoodkhani, U. Ali, P.D. Enrique, N.Y. Zhou, A. Bonakdar, E. Toyserkani, An investigation into the effect of process parameters on melt pool geometry, cell spacing, and grain refinement during laser powder bed fusion, Opt. Laser Technol. 116 (2019) 83–91.
[36] J. Shao, G. Yu, X. He, S. Li, R. Chen, Y. Zhao, Grain size evolution under different cooling rate in laser additive manufacturing of superalloy, Opt. Laser Technol. 119 (2019).
[37] H. Chen, Y. Lu, D. Luo, J. Lai, D. Liu, Epitaxial laser deposition of single crystal Ni-based superalloys: Repair of complex geometry, J. Mater. Process. Technol. 285 (2020).